NANO LETTERS
Letter
Cite This: Nano Lett. XXXX, XXX, XXX−XXX
pubs.acs.org/NanoLett

Selective Formation of Porous Pt Nanorods for Highly Electrochemically Efficient Neural Electrode Interfaces

Mehran Ganji,[†] Angelique C. Paulk,[‡] Jimmy C. Yang,[‡] Nasim W. Vahidi,[†] Sang Heon Lee,[†] Ren Liu,[†] Lorraine Hossain,[§] Ezequiel M. Arneodo,[∥] Martin Thunemann,[∥] Michiko Shigyo,[#] Atsunori Tanaka,[§] Sang Baek Ryu,[▽] Seung Woo Lee,[▽] Youngbin Tchoe,[†] Martin Marsala,[#] Anna Devor,[⊥] Daniel R. Cleary,[○] Joel R. Martin,[○] Hongseok Oh,[†] Vikash Gilja,[†] Timothy Q. Gentner,[∥] Shelley I. Fried,[▽,◆] Eric Halgren,[⊥] Sydney S. Cash,[‡] and Shadi A. Dayeh*[,†,‡,□]

[†]Department of Electrical and Computer Engineering, University of California San Diego La Jolla, California 92093, United States
[‡]Department of Neurology, Massachusetts General Hospital, Boston, Massachusetts 02114, United States
[§]Materials Science and Engineering Program, University of California San Diego, La Jolla, California 92093, United States
[∥]Department of Neurosciences, University of California San Diego, La Jolla, California 92093, United States
[⊥]Departments of Radiology and Neurosciences, University of California San Diego, La Jolla, California 92093, United States
[#]Department of Anesthesiology, University of California, San Diego (UCSD), La Jolla, California 92037, United States
[▽]Department of Neurosurgery, Massachusetts General Hospital, Boston, Massachusetts 02114, United States
[○]Department of Neurosurgery, University of California, San Diego (UCSD), La Jolla, California 92037, United States
[◆]Boston VA Healthcare System, 150 South Huntington Avenue, Boston, Massachusetts 02130, United States
[□]Department of Nanoengineering, University of California San Diego, La Jolla, California 92093, United States

Supporting Information

ABSTRACT: The enhanced electrochemical activity of nanostructured materials is readily exploited in energy devices, but their utility in scalable and human-compatible implantable neural interfaces can significantly advance the performance of clinical and research electrodes. We utilize low-temperature selective dealloying to develop scalable and biocompatible one-dimensional platinum nanorod (PtNR) arrays that exhibit superb electrochemical properties at various length scales, stability, and biocompatibility for high performance neurotechnologies. PtNR arrays record brain activity with cellular resolution from the cortical surfaces in birds and nonhuman primates. Significantly, strong modulation of surface recorded single unit activity by auditory stimuli is demonstrated in European Starling birds as well as the modulation of local field potentials in the visual cortex by light stimuli in a nonhuman primate and responses to electrical stimulation in mice. PtNRs record behaviorally and physiologically relevant neuronal dynamics from the surface of the brain with high spatiotemporal resolution, which paves the way for less invasive brain−machine interfaces.

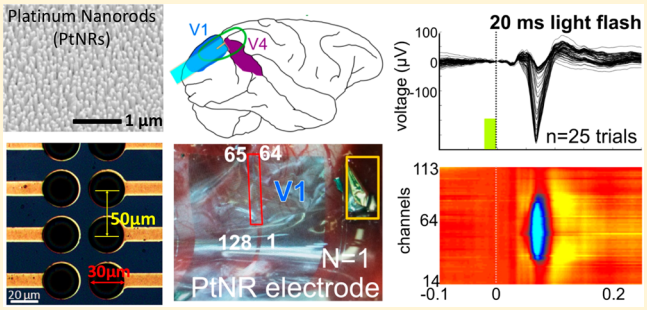

KEYWORDS: *platinum nanorod, clinical, brain, neural interface, neurotechnology*

One-dimensional (1D) nanowire structures have been utilized in measuring intracellular activity from individual cells,[1−4] and the extracellular activity from in vitro cultured tissue[5] as well as in vivo from intact retinal[6] and brain tissue.[7] One-dimensional nanostructures can be transferred or printed on flexible substrates, but vertically aligned 1D nanostructures with chemically inert interfaces that are epitaxial to the underlying substrate are mostly formed by vapor phase techniques that require high temperatures,[8,9] which are incompatible with flexible substrates. Solution growth methods are readily available to form 1D nanostructures,[10] but their applicability to platinum (Pt), a biocompatible material that is widely used in clinical practice, is yet to be demonstrated. Platinum 1D nanostructures are particularly attractive because they can offer large surface area for charge coupling, and the enhanced electric fields at their tips[11] together with the emergence of high-index crystalline facets at their circumference[12] facilitate reversible charge transfer at the electrode−tissue interface. Most commonly, 1D Pt nanostructures are

Received: June 5, 2019
Revised: July 21, 2019
Published: August 1, 2019

DOI: 10.1021/acs.nanolett.9b02296
Nano Lett. XXXX, XXX, XXX−XXX

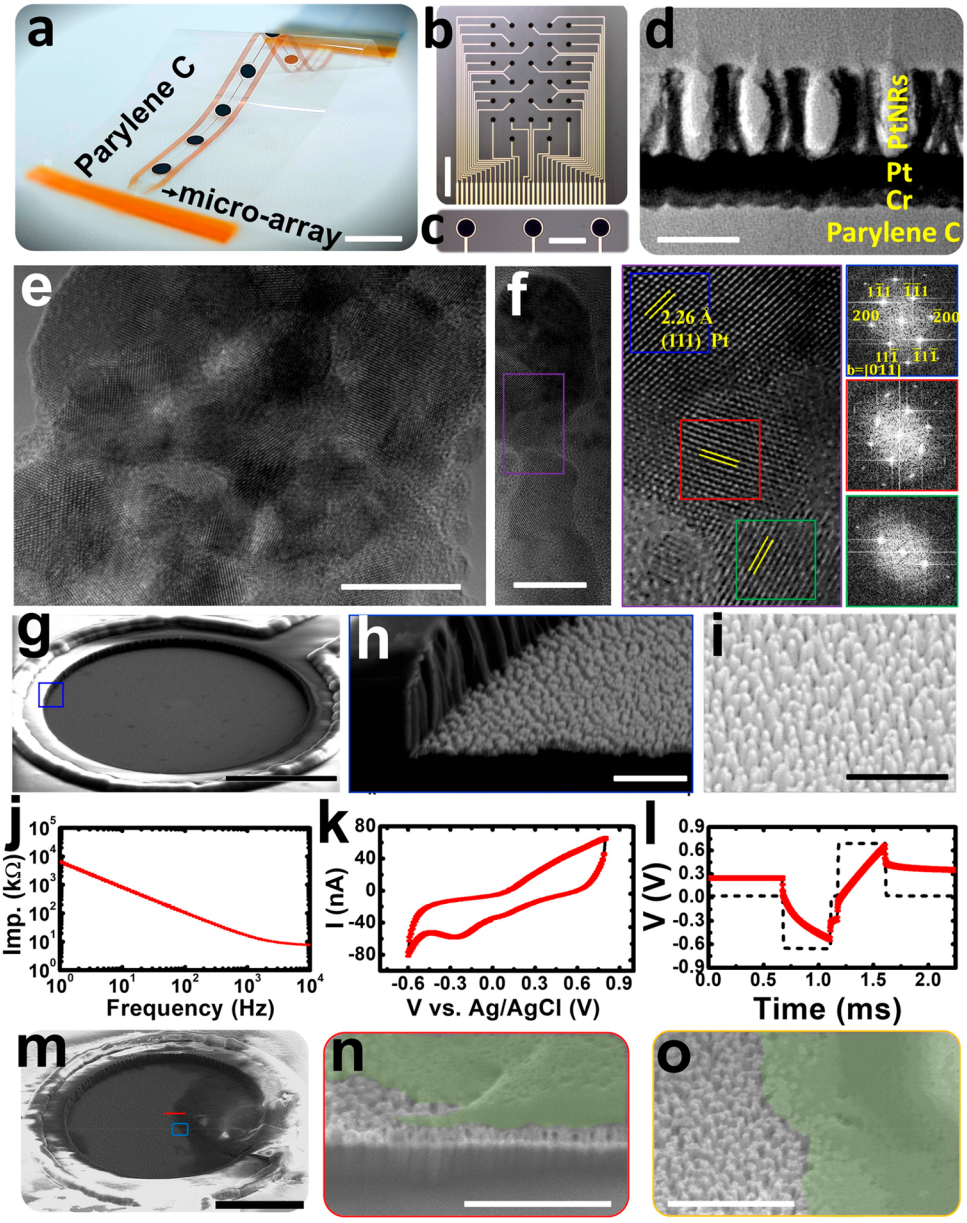

Figure 1. Structural, morphological, and electrochemical characterization of PtNR microelectrodes. (a) Picture of the fabricated electrophysiology PtNR device on thin film parylene C layer, showing the location of the PtNR microarray with 56 microelectrodes and six macro REF electrodes. Top view optical images of (b) PtNR array with 32 microelectrodes and (c) zoom-in images of three PtNR microelectrodes (D = 50 μm). (d) TEM image at the center of PtNR microelectrode, showing the cross-section of the stacked layers highlighting intimate contact between the different layers of the device. High-resolution TEM image at the center (e) and tip (f) of PtNR showing porous polycrystalline structure. Inset is fast Fourier transform (FFT) of the crystal planes showing multiple rotated spots indicative of the polycrystalline nature of the PtNR. (g–i) Tilted view SEM image of PtNR microelectrode (g) and cross-section (h) in the region highlighted with the black box in (g), and a zoom-in at the array center in (i). Average (black) and standard deviation (red) of measured electrochemical spectra for (j) impedance, (k) CV, and (l) voltage transients (injected biphasic current pulse I = 5 μA, PW = 400 μs) from 32 PtNR microelectrodes of the same device. (m) Top view SEM image of one explanted PtNR microelectrode, showing partial coverage with biological tissue. (n) Cross-sectional SEM image along red line in (m). (o) Tilted view zoom-in SEM image at the blue box in (m). Both (n) and (o) show similar PtNR morphology below tissue (n) and next to tissue (o). Scale markers are for (a) 10 mm, (b) 400 μm, (c) 100 μm, (d) 300 nm, (e,f) 10 nm, (g) 20 μm, (h,i) 2 μm, (m) 15 μm, (n) 2 μm, (o) 1 μm.

electrochemically deposited[13,14] or formed by dealloying Pt-containing metal compounds that usually result in PtNi,[15,16] PtAu,[17] or PtCo.[16,18] However, electrochemical methods lead to neither crystalline nanostructures nor to strong bonding to underlying metal leads due to incorporation of electrochemical surfactants in the nanostructures and at the interface with underlying metals, and thus have weak physical strength, similar to Pt-black. They can also be problematic due to toxic ligand additives, metal elements, and/or isotopes.[19]

To surmount these challenges, we developed a method for fabrication of Pt nanorods (PtNRs) using selective chemical dissolution of Ag from a cosputtered PtAg alloy on thin and flexible parylene C substrates (Figure 1a–c). The selective dissolution of metal alloys is known to result in nanoporous structures[20] and is optimized here (Figure S1) to result in 1D PtNRs as shown in the cross-sectional transmission electron microscopy (TEM) images taken at the center of a PtNR microelectrode (Figure 1d). The selective dealloying can result

DOI: 10.1021/acs.nanolett.9b02296
Nano Lett. XXXX, XXX, XXX–XXX

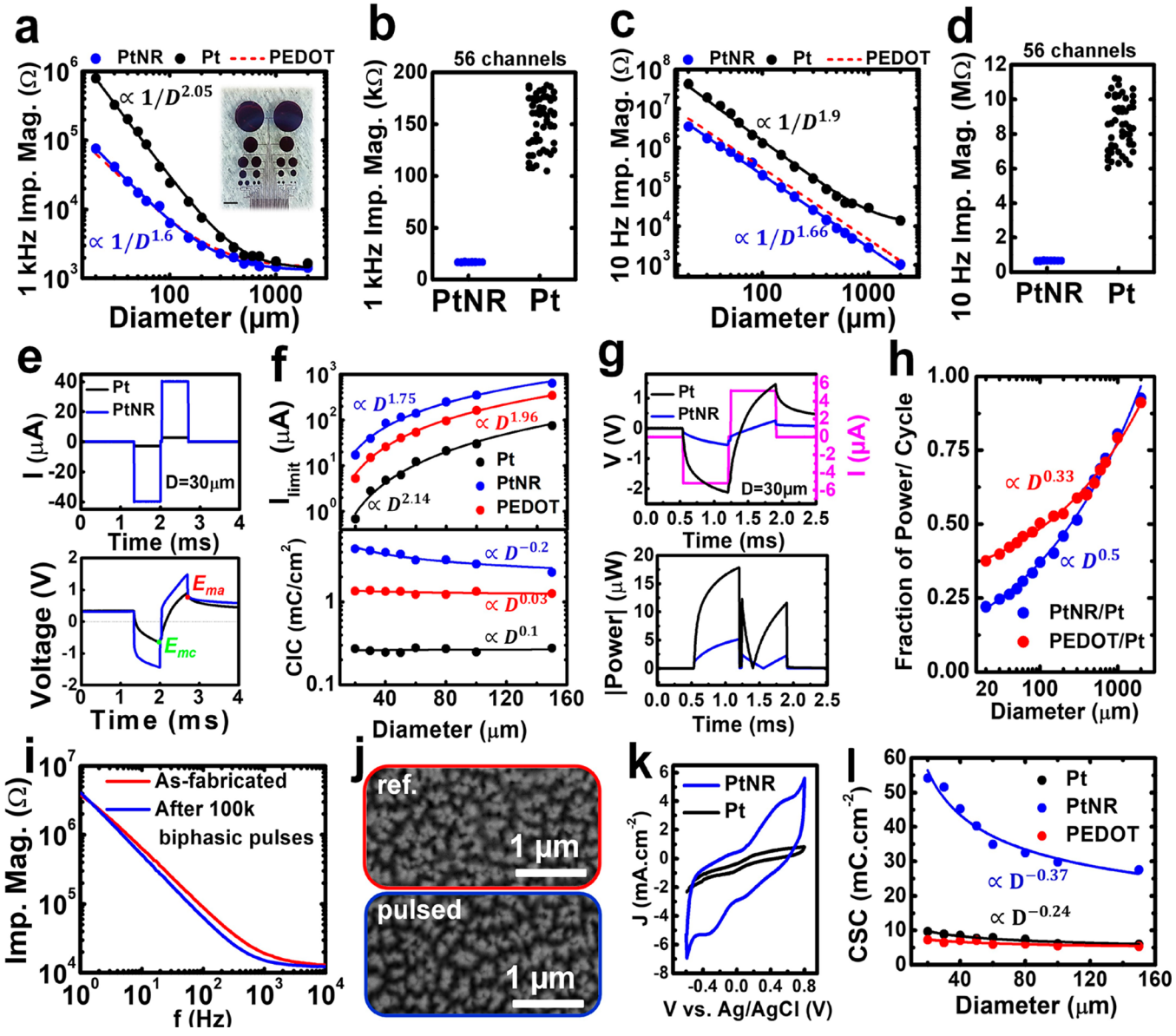

Figure 2. Electrochemical performance of PtNR vs Pt and PEDOT:PSS microelectrodes. (a) Measured and fitted values of electrochemical impedances of PtNR (blue), Pt (black), and PEDOT:PSS (red-dashed) as a function of diameter at 1 kHz. Note that PEDOT:PSS and PtNR are almost identically overlaid: (a) 1 kHz and 10 Hz (c). Inset in (a) shows the variable diameter electrode layout. Scatter plot of 1 kHz (b) and 10 Hz (d) impedances for 56 PtNR and Pt channels with 50 μm diameter. (e) Voltage transients in response to injected current (upper panel) for 30 μm diameter PtNR and Pt microelectrodes at their maximal (water hydrolysis) cathodal and the anodal potential limits. (f) Measured and fitted values of current injection limits and charge injection capacities as a function of diameter. (g) Measured voltage transients and calculated absolute power values of 30 μm diameter PtNR and Pt microelectrodes under the same charge injection (5 μA injected current). (h) Ratio of power consumption/cycle of PtNR and PEDOT:PSS microelectrodes in reference to activated planar Pt microelectrodes as a function of electrode size. The circles represent experimental measurements, and the lines are fits. (i) Impedance spectra of a 50 μm diameter PtNR microelectrode as-fabricated and after 100k biphasic current pulses (I = 50 μA, PW = 500 μs, f = 100 Hz). (j) Top view SEM images of PtNR on reference and 100k cycled microelectrode on the same array showing negligible morphological changes. (k) CV responses (current densities) with 30 μm diameter PtNR and Pt microelectrodes. (l) Charge storage capacities as a function of diameter showing superiority of PtNR microelectrodes.

in pure noble metals under elongated chemical etching or electrochemical biasing.[21] For our PtNRs, energy dispersive X-ray analysis showed that the 2 min dissolution resulted in 10% residual Ag atomic composition in the PtNRs (Figure S1d). The height of the PtNRs can be adjusted with the deposition time of the cosputtered PtAg alloy (Figure S2) and is chosen to be 300−400 nm for this work; a height that is sufficient to provide both high electrochemical performance and mechanical stability. The high-resolution TEM (HRTEM) images show that the PtNR is polycrystalline and porous (Figure 1e). The 1D porous structure (Figure 1e) provides large surface area, and the sharp corners of atomic steps at grain interfaces (Figure 1f) lead to large dipoles that enhance electrochemical coupling and reactions. The fabrication process for incorporating the nanorods onto planar underlying metal leads is described in the Methods Section and Supporting Information (Figure S3).

The optical microscope images of several microelectrodes (Figure 1b and Figure 1c) and the scanning electron microscope (SEM) images indicate uniform distribution of

DOI: 10.1021/acs.nanolett.9b02296
Nano Lett. XXXX, XXX, XXX−XXX

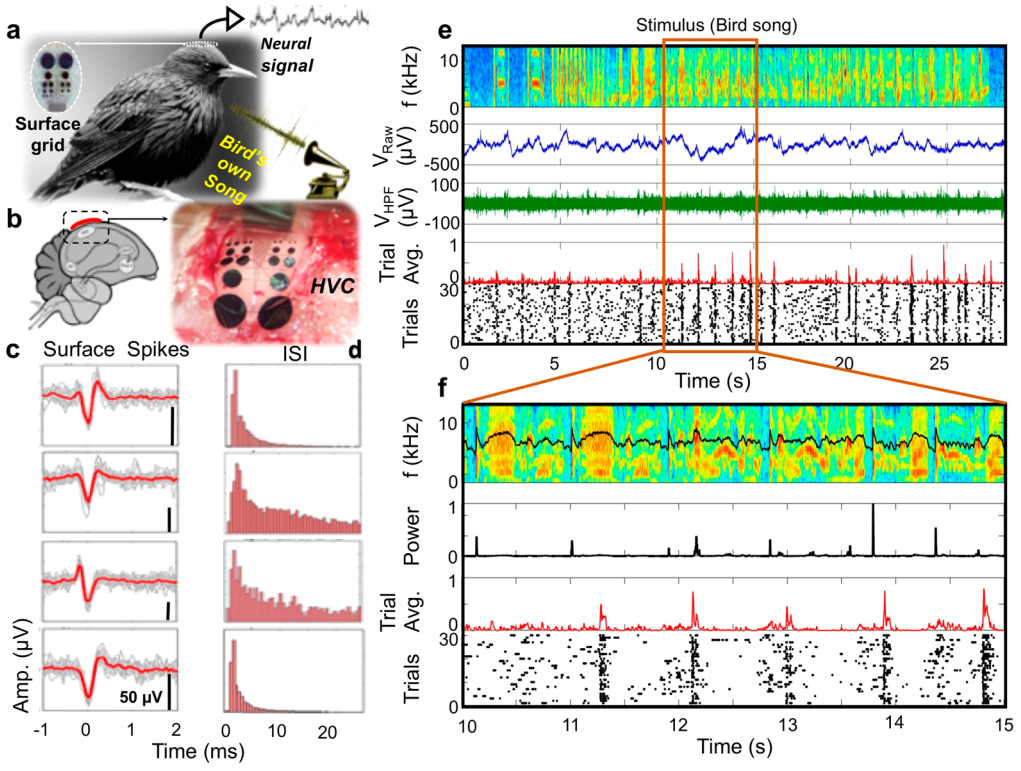

Figure 3. Recording of stimulus modulated single unit activity with PtNRs in songbird experiments (N = 1 Starling). (a) Auditory stimuli in the form of bird song (e.g., bird's-own-song) is played for European Starling bird under anesthesia and neural signals are recorded from HVC auditory area. (b) Schematic of the songbird brain circuit and location of PtNR array implant dorsal to HVC. (c) Example of single unit surface spike waveforms and (d) their corresponding interspike interval (ISI) histograms of waveforms recorded on four different contacts. The red waveforms are averages of 20 uniformly sampled spike snippets. The black scales on lower right of each waveform indicates 50 μV amplitude. (e) Surface recorded stimulus-driven neural response. First row shows the spectrogram of 28 s stimulus (bird's-own-song). Colors from blue to yellow indicate stimulus intensity from low to high over time. Second row displays a recorded raw voltage signal (blue). Third row demonstrates same signal high pass filtered (>300 Hz) (green). Fourth row shows trial averaged spike count (in 20 ms time bins) over 30 stimulus presentations. Bottom row is a spike raster plot showing individual time-locked spikes from an HVC single unit on 30 successive stimulus presentations. (f) Zoom in 5 s of stimuli: First row shows spectrogram of 5 s bird's-own-song. The log of power spectrum density (PSD) averaged over 65 frequency bands is overlaid as a black line. Second row is the average of 65 frequency bands of PSD. Third and fourth rows show the trial averaged and spike rate plots as in (e).

the PtNRs across a single microelectrode (Figure 1g). The PtNRs are beveled below the passivating parylene C layer at about 2 μm below the surface as shown in the cross-sectional SEM (Figure 1h) and tilted view SEM image (Figure 1i). This architecture significantly reduces the potential of PtNR damage due to shear forces that will be otherwise present if the PtNRs were to be fabricated on the device surface. The thin film fabrication process is of high-yield and uniformity, embodied in overlapping electrochemical impedance spectroscopy (EIS, Figure 1j), cyclic voltammetry (CV, Figure 1k), and voltage transients (VTs, Figure 1l) spectra across 32 microelectrodes in an example device (Figure 1b). To demonstrate the biocompatibility and mechanical stability of PtNRs in vivo, we implanted the device in the mouse cortex (Methods Section) for a period of 42 days followed by immunohistological staining (Figure S4) and examination of the explanted device by SEM (Figure 1m, Figure S5). Near normal neuronal and glial morphology and staining patterns were seen for implanted and contralateral nonimplanted sites in two mice (Figure S4). Several PtNR microcontacts were further sectioned by focused ion beam (FIB), and their cross-section (Figure 1n, Figure S5) showed intact PtNRs underneath the adsorbed tissue that remained on the microelectrode surface after explant. A higher magnification SEM image (Figure 1o) shows PtNR array morphology similar to that before implant (Figure 1h,i). Additionally, the compatibility of different sterilization techniques (autoclave, ethylene oxide (ETO), STERRAD) with PtNR electrodes was validated (Figure S7). Over 90% of the microelectrodes were functional with a slightly increased impedance magnitude after sterilization, but no morphological changes were observed, contrasting results we obtained on PEDOT:PSS with STERRAD sterilization.[22] These results demonstrate that PtNRs are biocompatible, robust, and suitable for clinical translation.

Further highlighting the electrochemical performance and stability of the PtNR electrodes, PtNR electrode impedances at 1 kHz in the diameter range of 20 μm to 2 mm are similar to those of PEDOT:PSS,[23] one of the most electrochemically efficient neural electrode materials and were lower than those of activated planar Pt microelectrodes (Figure 2a). Activation of PtNRs and planar Pt electrodes is achieved by 10 cycles of cyclic voltammetry. At 1 kHz, the impedance of PtNRs is 10× smaller than that of activated planar Pt microelectrodes at smaller diameters, whereas impedances of larger diameter microelectrodes become limited by their series resistances (Figure S6).[24] For a 56 microelectrode array with 50 μm diameter per site, the electrode impedance at 1 kHz for PtNRs is uniform (16.89 ± 0.47 kΩ) and is lower than the more variable impedances (153.01 ± 24 kΩ) of similar-diameter activated Pt microelectrodes (Figure 2b). The 10 Hz

DOI: 10.1021/acs.nanolett.9b02296
Nano Lett. XXXX, XXX, XXX−XXX

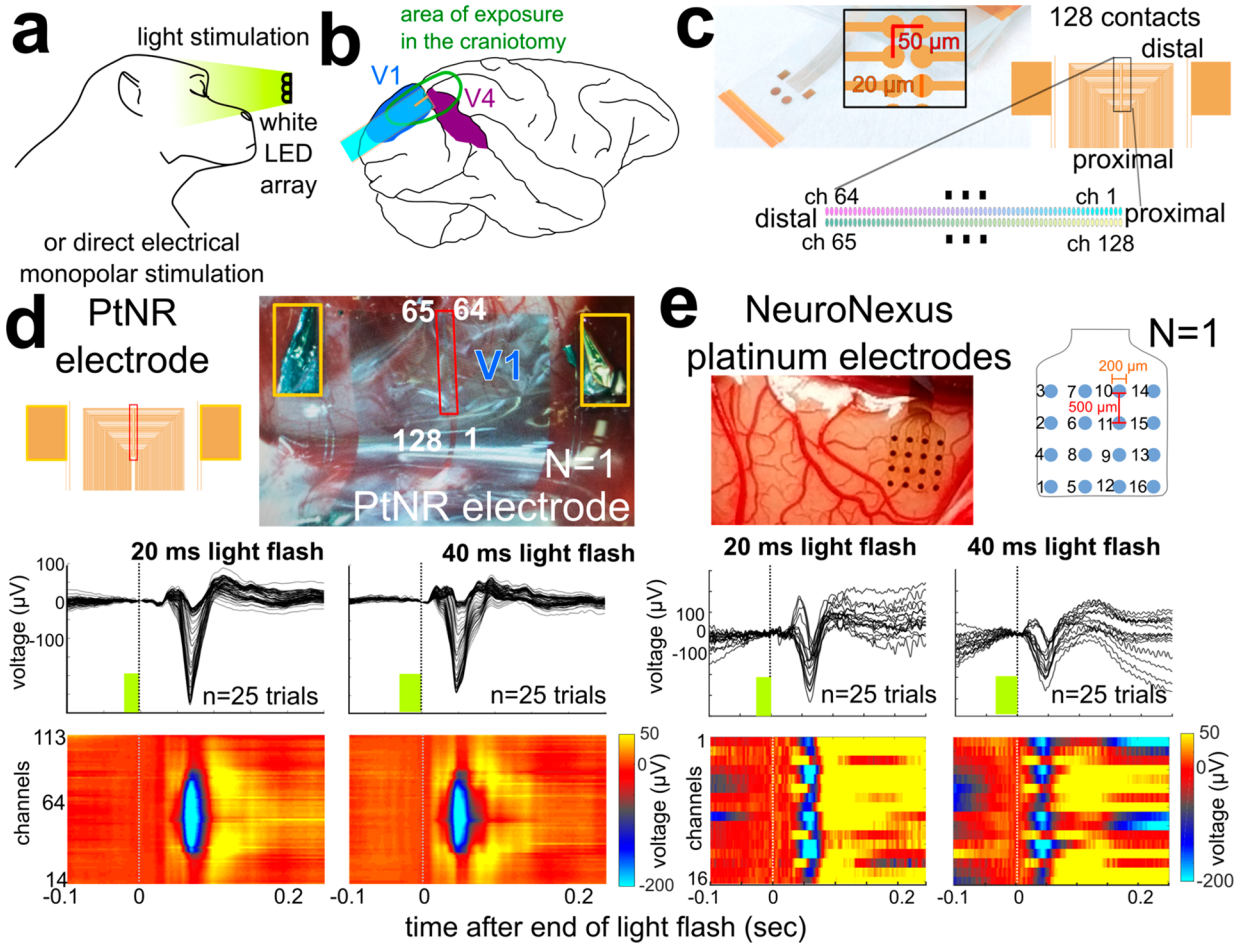

Figure 4. Recording of stimulus modulated local field potential dynamics with PtNRs in nonhuman primate experiments (N = 1). (a) Visual stimulation preparation involved anesthetized nonhuman primates (NHPs). (b) Schematic of the NHP brain and location of PtNR array implant in top of the primary visual cortex (V1). (c) Electrode map, which involves two columns of 64 channels. (d) PtNR recording on the NHP V1 cortex with an average visually evoked response to 20 ms (left) and 40 ms (right) duration light flashes, viewed across channels as averages (top traces) and as viewed across the spatial map (bottom). (e) Recording from V1 in the same cortex as (c) but with the platinum Neuronexus grid in the same area of V1 cortex.

electrochemical impedance for PtNRs is also significantly lower than that of activated planar Pt microelectrodes and lower than that of PEDOT:PSS microelectrodes for all studied diameters (Figure 2c). The impedance values are also relatively uniform for a fixed 50 μm diameter (0.670 ± 0.025 MΩ) compared to activated planar Pt microelectrodes (8.95 ± 2.1 MΩ; Figure 2d). The low impedance of PtNR microelectrodes across frequencies is essential for the high fidelity recording of a broad range of brain activity such as local field potentials (ranging from ~0 to 300 Hz) to single and multiunit activity >300 Hz.[25]

It has also become increasingly important to be able to use microelectrodes to modulate neural activity.[26] Stimulation capability is assessed by the charge injection capacity (CIC), the maximum amount of charge that can be injected through the electrode prior to building a potential across the electrode/electrolyte interface that can cause water hydrolysis (Figure 2e). For all diameters, PtNRs allow injection of higher currents and therefore permit higher CIC compared to PEDOT:PSS and activated planar Pt microelectrodes (Figure 2f). For a 20 μm diameter microelectrode, the CIC of PtNR is 4.4 mC·cm^{-2}, which is ~16 times larger than activated planar Pt (0.27 mC·cm^{-2}) with the same diameter. For the same current, the smaller voltage transients built across the PtNR/electrolyte interface lead to significantly smaller power dissipation per a single biphasic pulse (Figure 2g). This power can be as much as a quarter of that required to inject the same amount of charge across activated planar Pt microelectrodes (Figure 2h) and lower than that required for PEDOT:PSS microelectrodes. One hundred thousand biphasic current pulses effectively reduce the electrode impedance (21% reduction at 1 kHz; Figure 2i), presumably due to desorption of contaminants and H-plated adsorption sites on the electrode surface without influencing the structure of the PtNRs (as inferred from the SEM images in Figure 2j). The charge storage capacity (CSC) deduced from the integrated area under the CV spectra (Figure 2k) demonstrate superior values that are 6 and 8 times larger than those of activated planar Pt and PEDOT:PSS microelectrodes, respectively, due to the high surface area of the PtNRs (Figure 2l). Overall, based on our quantitative assessments of the devices, the PtNR microelectrode system is a robust system for high performance, safe, and stable neural electrode interfaces.

To demonstrate the superior neural recording capabilities of PtNR microelectrodes, we recorded from cortical regions in songbirds (Figure 3) and from the visual cortex of a nonhuman primate (Figure 4). Similar to PEDOT:PSS microelectrodes,[23]

DOI: 10.1021/acs.nanolett.9b02296
Nano Lett. XXXX, XXX, XXX−XXX

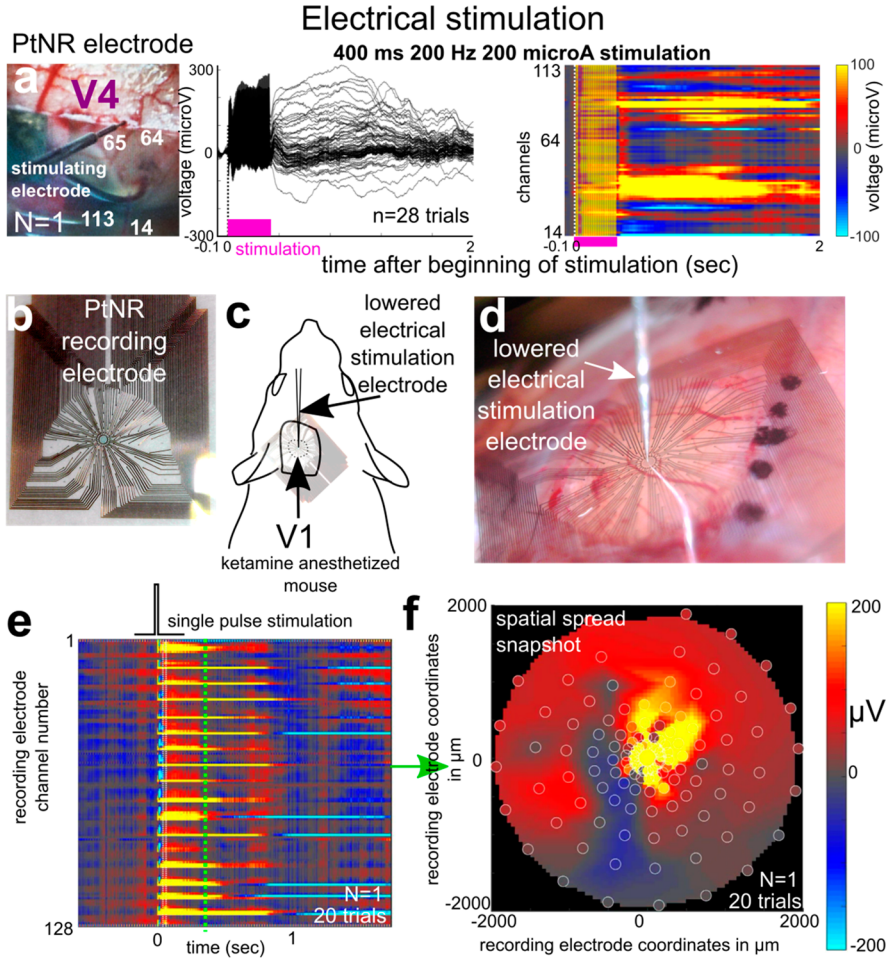

Figure 5. Recording of stimulus modulated local field potential dynamics with PtNRs in mouse experiments (N = 1 NHP and N = 1 mouse). (a) Electrical stimulation responses to 400 ms train of 200 Hz, 200 μA of stimulation near the PtNR array in V4 in a second NHP (left), with the average responses across channels showing responses up to 2 s after stimulation (middle), which are distributed across the array (right). (b) Electrode map, which involves concentric rings of electrode contacts. (c) Electrical stimulation preparation involved a ketamine-anesthetized mouse. Schematic of the mouse and location of PtNR array implant on top of the primary visual cortex (V1) and (d) an image of the preparation on the mouse cortex. (e) PtNR recording on the mouse V1 with an average electrically evoked response to a single pulse (30 μA) of monopolar electrical stimulation via the lowered depth electrode. Responses at the center of the PtNR array in V1, with the average responses across channels showing responses up to 2 s after stimulation (middle). (f) These responses are distributed across the array as captured at a specific moment in time (green line in (e)). The map was interpolated across electrode sites as indicated by the circles on the array.

we found PtNRs can capture well isolated action potentials from single neurons (i.e., single units) from the cortical surface. When the electrode is implanted over the sensorimotor region HVC (used as a proper name) of the starling (Figure 3a,b), threshold waveform events evident in the high pass filtered data (Figure S8; bird in Figure S8; and Figure S9 is different from Starling in Figure 3) could be clustered, resulting in putative single unit waveforms with interspike interval (ISI) distributions consistent with the published literature (Figure 3c). To confirm the presence of single unit action potentials, a silicon depth electrode (NeuroNexus Technologies, Inc.) was inserted through the surface microarray, allowing simultaneous recordings of surface and depth units (Figure S9). Significantly, we observed stimulus-locked modulation of the single unit activity to auditory stimuli across multiple trials from the HVC, indicating coordinated single unit and population-level activity measured from the surface of the brain (Figure 3e). Figure 3 shows the specific pattern of firing observed in one example neuron recorded with the PtNR microelectrode in response to the bird's-own-song. Consistent responses are observed in the raw measured potentials, the high pass filtered (HPF) waveform, the trial averages, and the single unit raster plot from the 30 trials. Zooming in on a 5 s segment of the recording illustrates that this firing is time-locked to the auditory stimuli (Figure 3f), but does not align directly with peaks in the spectral power. Recordings with PtNR microelectrodes are of high quality enabling us to extract low noise receptive fields (Figure S10). The cellular resolution and responses of single units to relevant external stimuli highlight the potential for the use of thin PtNR microelectrodes in minimally invasive neuroprosthetic applications.

To test how well the PtNR electrodes could detect behaviorally and physiologically relevant local field potential dynamics, we recorded neural responses in the primary visual cortex (V1) to light flashes delivered to an anesthetized nonhuman primate (NHP; N = 1; Figure 4a–e). We examined the average visual responses across a 2-column array of electrodes and found large visually evoked potential (VEP) responses 0.1 s after either 20 or 40 ms duration light flashes (Figure 4c,d). The duration of the average VEPs were longer

DOI: 10.1021/acs.nanolett.9b02296
Nano Lett. XXXX, XXX, XXX−XXX

with the longer duration light flash, with a stronger response toward the end of the 2-column electrode array. We compared how well the PtNR electrodes recorded VEPs compared to a grid of conventional platinum (NeuroNexus, Figure 4e) and found the responses were larger with the PtNR electrode, with significantly less noise as averaged across >20 trials per channel (Figure 4d,e). We also examined the neural response to electrical stimulation in the nonhuman primate and mouse cortex (Figure 5; NHP in Figure 4 is different from the NHP in Figure 5). Using lowered monopolar micro depth electrodes, we stimulated visual areas and recorded the neural responses using the PtNR electrodes. We observed large voltage responses to trains (Figure 5a) and single pulses (Figure 5e,f) of stimulation, which could be localized in time and space across a 2-column array as well as a circular array of PtNR electrodes (Figure 5e-f).

In summary, we developed a Pt-based biocompatible electrode system, PtNRs, whose electrochemical performance surpasses those of currently pursued electrode materials for neural interfaces. Across species, PtNRs microelectrodes are capable of recording detailed broadband neuronal activity with high spatiotemporal resolution in response to auditory, visual, and electrical stimulation. These results demonstrate the great potential for clinical translation evidenced by their excellent electrochemical properties, their biocompatibility, and their stability. In addition to high-quality neuronal recordings reported here, the excellent stimulation capability of PtNRs extend beyond cortical implants to applications for intervention with the spinal cord and peripheral nervous system.

METHODS

Device Fabrication. The fabrication of the PEDOT:PSS and Pt devices is similar to previously established protocols.[27−29] For PtNRs, glass slides (Specialty Glass Products Inc.) or silicon wafers were used as substrate carriers for the thin parylene C layers. The substrates were first solvent cleaned by rinsing with acetone/isopropanol (IPA)/deionized (DI) water/IPA, then were subjected to ultrasonic agitation in IPA for 5 min and rinsed again with acetone/IPA/DI water/IPA. Diluted Micro-90 (0.1%), an antiadhesion layer, was spun-cast at 1500 rpm on the substrate to facilitate the separation of the device after the device fabrication was completed. A first parylene C layer (∼1.9−2.5 μm) was deposited by chemical vapor deposition using a PDS 2010 Parylene coater system. Metal lead patterns were defined and exposed using a Karl Suss MA6 mask aligner using NR9-3000 negative resist. Temescal BJD 1800 electron beam evaporator was used for the deposition of 15 nm Cr adhesion layer and 100 nm Au contact layer, and a lift-off process in acetone followed. Then patterns of the electrode sites were defined using NR9-6000 negative resist and a Karl Suss MA6 mask aligner for exposure. A 15 nm/100 nm Cr/Pt layer was sputtered followed by deposition of ∼0.5 μm thick PtAg alloy using a cosputtering technique performed at 400 W (RF) and 50 W (DC) powers for codeposition of Ag and Pt, respectively. A lift-off process in acetone followed shortly after. To realize PtNR film on electrode sites, dealloying was performed in nitric acid at 60 °C for 2 min. O_2 plasma (Oxford Plasmalab 80 RIE) was then applied for 2 min (150 W RF power) to activate the surface of parylene C for enhancing the adhesion of the subsequent encapsulating parylene C layer. A layer of ∼1.9−2.5 μm parylene C was then deposited and followed by coating another Micro 90 antiadhesion layer. This time, a slightly higher concentrated Micro-90 (1% as opposed to 0.1% for the first layer) was spun-cast at 650 rpm for 10 s on this second parylene C layer for ease of separation of the subsequent layers. A third parylene-C layer was then deposited to serve as a protector film for passivation layer during etching the electrode sites opening. Then a thick 2010 SU-8 photoresist was spun-cast and patterned, which was exposed and developed with SU-8 developer. O_2 plasma was used to etch the openings in the third and second parylene C layers. The third parylene C layer was then mechanically peeled off in all regions, resulting in exposure of fresh passivation layer (2nd PXC layer) and PtNR contacts as only interface materials. Finally, the devices were immersed in DI water to remove any Micro-90 residue from the PtNRs and parylene C surface, where bonding to anisotropic conductive film (ACF) and commercial off the shelf ribbon cables, for external circuitry connection, completed the fabrication of PtNR electrophysiology devices.

Device Characterization. The devices were imaged using Axioscope Optical microscope and FEI SFEG ultra high-resolution SEM at 10 kV accelerating voltage. To reduce electron charging in the specimen, a 15 nm thick Ti layer was deposited on the back of the device and was electrically connected to the stage of the system providing a runaway path for impinging electrons. To obtain the TEM images, focused ion beam (FIB) was used to create cross-sectional slices of the microelectrodes. To prevent the sample from the damage by ion beam during the FIB milling process, the fabricated device is deposited with 1 μm SiN_x by Trion Orion III chemical vapor deposition (CVD) system. After that, the sample was coated with a 30 nm Pt layer by e-beam evaporation to reduce the charging under electron and ion beams. The TEM sample lamellae was prepared with FIB (FEI Nova 600). The FIB and in situ lift-off (INLO) process utilized here follow conventional procedures in which a 30 keV Ga beam was used for rough milling and reduced voltage (10 keV) was used for fine milling. TEM characterization was carried out using a FEI Tecnai G(2) F30 S-Twin 300 kV transmission electron microscope, equipped with Fischione Instruments high angle annular dark field (HAADF) and EDAX ECON energy-dispersion X-ray (EDX) detectors under scanning TEM (STEM) mode. These experiments were performed at the Center for Integrated Nanotechnologies at Sandia National Laboratories.

EIS was performed using a GAMRY interface 1000E in 0.01 M phosphate buffer saline (×1 PBS) solution, using three electrodes configuration, i.e., Ag/AgCl electrode as a reference electrode, a large platinum electrode as a counter electrode, and the target micro/macrodot arrays as the working electrode. Sinusoidal signals with 10 mV RMS AC voltage and zero DC bias were applied, and the frequency was swept from 1 Hz to 10 kHz. The cyclic voltammetry was performed under low current density, near equilibrium conditions in (1 ×) PBS solution, whereas tested electrode potential was swept cyclically between potential limits of −0.6 to 0.8 V vs Ag/AgCl at constant scan rate of 200 mV s^{-1} with 10 mV potential steps. The CSC_C and CSC_A were calculated by time integral of the cathodal and anodal current density over a potential range of water electrolysis window for each material. To calculate the charge injection capacity, cathodal-first, biphasic, charge-balanced current pulse were injected across working electrode and counter electrode while measuring working electrode's polarization potential with respect to Ag/AgCl reference electrode. The maximum cathodal excursion potential (E_{mc}) and anodal excursion potential (E_{ma}) were calculated as

DOI: 10.1021/acs.nanolett.9b02296
Nano Lett. XXXX, XXX, XXX−XXX

electrode potential versus Ag/AgCl (reference electrode) 10 μs after cathodal and anodal pulses ended. This period of interpulse delay is used to account for the voltage drop across the electrolyte and metal lead series resistance, resulting in an absolute polarized potential across electrode/electrolyte interface versus Ag/AgCl. Charge injection capacity was calculated as the injected charge (by multiplying stimulation current and pulse width) at which either E_{mc} reaches water reduction potential (cathodal limit) and/or E_{ma} reaches water oxidation potential (anodal limit). Water window limits are considered between −0.6 to 0.8 V for metallic electrodes (Pt and PtNR) and −0.9 to 0.6 V for organic electrodes (PEDOT:PSS), with respect to Ag/AgCl reference electrode. To maintain different interpulse potential (E_{ipp}) bias for each electrode materials, a net current flowed across the electrode/electrolyte interface with minute current magnitude (typically <10 nA) even for millimeter scale electrodes.

Bird Surgical Details and Recording Methods. Preparatory surgeries were conducted either the day before or the day of electrophysiological recording. Animals were anesthetized with isoflurane (Baxter Healthcare). The birds were head-fixed in a stereotaxic device, and the scalp was dissected along the midline. A custom-built, metallic fixation pin was then attached to the caudal part of the bird's skull with dental cement.

On the days of recordings, an animal was anesthetized with 20% urethane (60−100 μL total; Sigma, St. Louis, MO) administered into the pectoral muscle in 20- to 30-μL aliquots at 30 min intervals. The bird was placed in a sound-attenuating chamber, and its head was immobilized via the head-fixation pin.

These experiments were performed on two adult European starling songbirds and two zebra finches under a protocol approved by the Institutional Animal Care and Use Committee of the University of California, San Diego. A craniotomy and duratomy was performed over HVC, following stereotaxic coordinates. The window was centered at 2.5 mm lateral and was large enough to fit the surface micro-ECoG array. The hippocampus on top of HVC was removed by suction. To ensure intimate contact between the surface array and tissue, cerebrospinal fluid was aspirated from the surface of the brain by suction. The surface array was then placed on top of the brain using a micromanipulator (Narishige MO-10), and the depth probe was slowly lowered into the brain through one of the two via perforations in the array. Both hemispheres of the brain were used; whenever the brain tissue was visibly damaged by the procedure, the site was not further used for the experiment.

Electrophysiological recordings from both the surface array and depth probe were performed simultaneously with the same data acquisition system, Intan RHD2000 from Intan Technologies (Los Angeles, CA). The Intan RHD2000 USB Controller was connected to a RHD2116 or RHD2132 headstage that was connected to the depth probe; a separate RHD2164 headstage was connected to a surface probe. The following adapter boards were used to connect the probe to the Intan headstage: a custom Flex Adapter[30] for the surface probe and a Plexon (Dallas, TX) N2T A32-HST/32 V adapter for the depth probe. Recordings were sampled at either 20 kHz or 30 kHz, and data was acquired using either the Open Ephys GUI[31] or RHD2000 software provided by Intan. Intan filter settings were used with cutoffs set at 0.01 Hz and 7.5 kHz for data acquisition.

Stimuli were played using software written in Python, running on a single board computer (SBC) (Beaglebone Black). Synchronization with the recording system and later identification of the metadata of the stimuli was achieved by digital trigger pins and/or messages passed using the ZMQ library between the SBC and the Open Ephys recording software. To enable high precision of stimulus onset detection in the recordings, the stimuli were stereo, with one channel containing a 1−5 kHz waveform that was recorded by the Intan system at the same sampling rate as the neural data. (The software is available on: https://github.com/zekearneodo/ephysflow/tree/master/rig_tools.)

Spike sorting and clustering were performed using KiloSort software. Clusters were then sorted into three groups, namely, single unit (SUA), multiunit (MUA), and "noise", based on their refractory period. Clusters with little to no spikes 0 to 2 ms from the previous spike were considered single unit. Clusters containing many spikes with a refractory period of less than 2 ms were considered multiunit.

NHP Surgical Details and Recording Methods. Experimental procedures on rhesus macaques were carried out in accordance with the Guide to the Care and Use of Laboratory Animals. All efforts were made to minimize discomfort, and the Institutional Animal Care and Use Committee at the Massachusetts General Hospital monitored care and approved all procedures.

Intraoperative, intracranial neurophysiology recordings were acquired from two adult male rhesus macaques (*Macaca mulatta*, ages 11 and 14). Macaques were placed under general endotracheal anesthesia (isoflurane) and placed into a stereotactic frame (Kopf; Kujunga, CA). Craniotomies over the visual cortex were performed using standard anatomic landmarks, and cortex was carefully exposed. Using gyral anatomy and vasculature over V1 versus V4 (Figure 4), V1 and V4 areas were identified visually, and PtNR electrodes were placed over each region. Signals were recorded using the Intan Recording System as described previously, similar to what was used in gathering the starling data. The data from the PtNRs was acquired at 30 kHz and filtered by default Intan settings with cutoffs of 1 Hz to 7.5 kHz. The majority of the data was acquired using OpenEphys acquisition graphic-user interface software[31] (http://www.open-ephys.org/), with the impedance tests of the electrodes during the experiments carried out using the Intan RHD2000 software from Intan Technologies (Los Angeles, CA). Data was extracted and processed using MATLAB (Mathworks, Natick, MA). The data from the Pt NeuroNexus ECoG electrode (model E16-500-5-200-H16) was recorded using an amplifier (Model 3500, A-M Systems) and a data acquisition system (Micro 1401-3, CED) with software (Spike 2,CED). The data was acquired at a sampling rate was 25 kHz and filtered by amplifier settings with cutoffs of 0.3 Hz to 10 kHz.

Data recorded from PtNRs and from NeuroNexus Pt electrodes were both downsampled to 1000 Hz and low pass filtered below 200 Hz. To make the voltage signals as similar as possible, we also high pass filtered the Neuronexus recording at 1 Hz, which is the same filter setting as used with OpenEphys. Further, 60 Hz noise was removed by subtracting the bandpass filtered signal from the original voltage traces. The power plots were calculated using Morlet wavelet transforms with custom analysis code in MATLAB and Fieldtrip (Oostenveld et al., 2011; http://www.ru.nl/neuroimaging/fieldtrip).

DOI: 10.1021/acs.nanolett.9b02296
Nano Lett. XXXX, XXX, XXX−XXX

For visual evoked potential experiments, an LED array comprising white LEDs (Cree; Durham, NC) was placed over each closed eye and secured in place. A general anesthetic regimen of propofol and fentanyl was used briefly to facilitate the recording of visual evoked potentials. Twenty or 40 ms full-field flashes at 1 Hz were delivered via TTL and computer-controlled software (LabView, National Instruments).

Mouse Surgical Details and Recording Methods. The care and use of mice (2−6 months old; C57BL/6J; Jackson Laboratory, Bar Harbor, ME) followed all federal and institutional guidelines, and the Institutional Animal Care and Use Committees of the Massachusetts General Hospital. Mice were deeply anesthetized with a cocktail of ketamine hydrochloride (100 mg/kg intraperitoneal injection) and xylazine (10 mg/kg intraperitoneal injection) prior to the start of surgery. Additional ketamine (1/10 initial dose) was supplemented every 30 min to maintain the plane of anesthesia.

Anesthetized mice were placed into a stereotaxic frame (Narishige, Japan) for the craniotomy as well as all subsequent testing. A heating blanket on the floor of the frame was used to maintain body temperature at 37 °C. A 4.5 mm × 4.5 mm craniotomy was performed on the area around the primary visual cortex (V1) defined by a stereotaxic coordinate[32] (AP: −3.8, ML: −2 mm). After the craniotomy, the PtNR array was placed over the exposed visual cortex. Once the PtNR array was positioned on V1, neural signals were recorded using the Intan Recording System. Similar to the recordings in NHPs, data was acquired at 30 kHz and filtered by the Intan setting (cutoffs of 1 Hz to 7.5 kHz). Data was extracted and processed using MATLAB.

In addition to the stereotaxic coordinate, the location of the array on V1 was confirmed again by measuring visually evoked potentials using full-field visual stimulation. Visual stimulation was presented from a monitor (HP ZR22w, Hewlett-Packard, USA) placed 25 cm from the mouse with a viewing angle of 45° from the center of the monitor (toward the right eye of the mouse). The stimulus was delivered at least 30 times, and the recording data from each trial were averaged. After confirming the array location, a monopolar stimulating electrode (10 KΩ; PI2PT30.01A10; Microprobes) was inserted into the visual cortex through the hole in the center of the PtNR array (Figure S10d). Electrical stimulation consisted of a 200 μs, 10−30 μA cathodic first biphasic current pulse with no interphase-interval (i.e., 1 pulse was delivered every 3 s). Each electric stimulus was delivered 20 times, and the recording data across trials were averaged.

Analysis and Statistical Methods. The spike waveforms (Figure 3c, Figure S9) are extracted from single unit clusters in Kilosort. The red waveforms are averages of 20 uniformly sampled spike snippets. The black scales on the lower right of each waveforms indicates 50 μV amplitude. The interspike intervals (ISI) is the time between succeeding spikes of a neuron. The ISI histogram of spike waveforms shown in these figures indicate the distribution of the log of ISI, which can be a visual tool to track violation of refractory period and differentiate single cells from multiunit. Besides extracting waveforms from clusters, we can examine their quality and whether they are related to real neural cells or noise. One way to conduct this test is to monitor cell activity in response to stimulus with repeated trials. If a single unit response shows any stimulus locking property, this can be an indication of an isolated neuron. Figure 3e is an example of a recorded cell from the surface of the brain with a stimulus locking response over 30 trials. The first row shows the spectrogram of a 28 s bird's-own-song stimulus. To create this spectrogram, bird song is converted to spectrograms by use of the MATLAB spectrogram function with parameters nfft = 128, and Hanning window of nfft with 50% overlap. It contains 65 frequency bands in range 0−10 kHz. The second row shows an example of one channel (Ch1) raw data in blue. The raw data contains both low and high frequency information. The green wave underneath is the high pass filtered (>300 Hz) raw data and contains spikes. At the bottom, the 30 trials average and raster plot of spike trains in response to 30 song trails have been shown. Figure 3f has zoomed-in view of 5 s from Figure 3e. In this figure on the spectrogram plot, logarithm of power spectral density (PSD) averaged over 65 frequency bands of spectrogram is shown in black. Underneath in black, average of 65 frequency bands of PSD is calculated for 5 s stimulus.

Local field potential recordings from nonhuman primates were extracted into MATLAB decimated to 1000 Hz. Voltage responses were averaged across trials of light flashes or pulses or trains of electrical stimulation.

Histology. The mice were perfused with 0.9% saline followed by 4% paraformaldehyde (PFA) in PBS. After microgrids were removed carefully from the brain surface by using tweezers, the brain was dissected from skull and postfixed in 4% PFA overnight at 4 °C. Tissue was then cryoprotected in 30% sucrose overnight. Coronal brain sections cut on a cryostat with 30 μm per slice were performed immunostaining. Sections were incubated with primary antibodies to detect neuron (NeuN, 1:500, Millipore, cat#ABN91), astrocyte (Cy3 fluorescence conjugated-GFAP, 1:1000, SIGMA-Aldrich cat#C9205), and microglia (Iba1, 1:1000, Wako cat#019−19741) in 5% normal donkey serum containing 0.3% triton X-100-containing PBS at 4 °C overnight. Following washing in PBS, sections were incubated with donkey anti chicken Alexa Fluor 488 and donkey anti rabbit Alexa Fluor 647 in 0.3% triton X-100-containing PBS. Sections were then mounted on glass slides, dried at room temperature, and covered with DAPI-containing Prolong antifade kit. Images were captured using an apotome equipped fluorescent microscopy on a Zeiss AxioImager.

■ ASSOCIATED CONTENT

Supporting Information

The Supporting Information is available free of charge on the ACS Publications website at DOI: 10.1021/acs.nanolett.9b02296.

Detailed information regarding the alloy deposition/dealloying and fabrication steps, the energy dispersive X-ray spectral characterization, histology on chronically implanted mice and characterization of explanted electrodes, electrochemical impedance spectroscopy and their small signal components, sterilization effects of autoclave, ethylene oxide, and sterrad, on impedance distribution, comparison of surface and depth recorded single units and extracted composite receptive fields in songbird experiments, and comparison of recordings using PtNR devices and NeuroNexus ECoG Pt electrodes on NHP and corresponding power-frequency plots (PDF)

DOI: 10.1021/acs.nanolett.9b02296
Nano Lett. XXXX, XXX, XXX−XXX

AUTHOR INFORMATION

Corresponding Author

*(S.A.D.) E-mail: sdayeh@eng.ucsd.edu.

ORCID

Shadi A. Dayeh: 0000-0002-1756-1774

Author Contributions

S.A.D. conceived the idea, led the project and analysis, and wrote the manuscript. M.G. fabricated and optimized the devices and performed electrochemical characterization and analysis. S.H.L. and A.T. assisted in the fabrication and SEM, and R.L. performed the TEM. L.H. and E.M.A. performed the Starling experiments, and N.V. and T.G. performed analysis. M.T. and A.D. performed chronic mouse implant, and M.S. and M.M. performed histology. H.O. contributed to the interface electronics. Y.T. performed the EDX. D.R.C., J.R.M., V.G., and E.H. contributed to the experimental design and analysis. All authors contributed to the manuscript writing.

Notes

The authors declare the following competing financial interest(s): UC San Diego has filed a patent application based on this work: Platinum nanorod electrode arrays for highly sensitive and initiative brain-machine interfaces.

ACKNOWLEDGMENTS

The authors acknowledge the support of nano3 fabrication facilities and staff and also acknowledge the support of Dr. John Nogan and Dr. Katherine Jungjohann at the Center for Integrated Nanotechnologies (CINT) where TEM characterization was performed. The work was performed in part at the CINT, U.S. Department of Energy, Office of Basic Energy Sciences User Facility at Los Alamos National Laboratory (Contract No. DE-AC52-06NA25396), and Sandia National Laboratories (Contract No. DE-AC04-94AL85000). This work was performed in part at the San Diego Nanotechnology Infrastructure (SDNI) of UCSD, a member of the National Nanotechnology Coordinated Infrastructure, which is supported by the National Science Foundation (Grant ECCS-1542148). This work was supported in part by an NSF-CAREER award #1351980, NSF CMMI award #1728497, NSF-ECCS EAGER award #1743694, NIH/NINDS U01-099700 and 3R01MH111359, NIH/NEI R01-029022, and by the Center for Brain Activity Mapping at UCSD. R.L. was supported through a UC-National Lab in-residence graduate fellowship, and by the Center for Design-Enabled Nanofabrication (C-DEN) at the University of California.

REFERENCES

(1) Tian, B.; Cohen-Karni, T.; Qing, Q.; Duan, X.; Xie, P.; Lieber, C. M. Three-dimensional, flexible nanoscale field-effect transistors as localized bioprobes. *Science* **2010**, *329* (5993), 830−834.

(2) Xie, C.; Lin, Z.; Hanson, L.; Cui, Y.; Cui, B. Intracellular recording of action potentials by nanopillar electroporation. *Nat. Nanotechnol.* **2012**, *7* (3), 185−190.

(3) Robinson, J. T.; Jorgolli, M.; Shalek, A. K.; Yoon, M.-H.; Gertner, R. S.; Park, H. Vertical nanowire electrode arrays as a scalable platform for intracellular interfacing to neuronal circuits. *Nat. Nanotechnol.* **2012**, *7* (3), 180−184.

(4) Liu, R.; Chen, R.; Elthakeb, A. T.; Lee, S. H.; Hinckley, S.; Khraiche, M. L.; Scott, J.; Pre, D.; Hwang, Y.; Tanaka, A. High density individually addressable nanowire arrays record intracellular activity from primary rodent and human stem cell derived neurons. *Nano Lett.* **2017**, *17* (5), 2757−2764.

(5) Dai, X.; Zhou, W.; Gao, T.; Liu, J.; Lieber, C. M. Three-dimensional mapping and regulation of action potential propagation in nanoelectronics-innervated tissues. *Nat. Nanotechnol.* **2016**, *11* (9), 776.

(6) Hong, G.; Fu, T.-M.; Qiao, M.; Viveros, R. D.; Yang, X.; Zhou, T.; Lee, J. M.; Park, H.-G.; Sanes, J. R.; Lieber, C. M. A method for single-neuron chronic recording from the retina in awake mice. *Science* **2018**, *360* (6396), 1447−1451.

(7) Fu, T.-M.; Hong, G.; Viveros, R. D.; Zhou, T.; Lieber, C. M. Highly scalable multichannel mesh electronics for stable chronic brain electrophysiology. *Proc. Natl. Acad. Sci. U. S. A.* **2017**, *114* (47), E10046−E10055.

(8) Wagner, R.; Ellis, W. Vapor-liquid-solid mechanism of single crystal growth. *Appl. Phys. Lett.* **1964**, *4* (5), 89−90.

(9) Sun, G.; Xu, J.; Harrowell, P. The mechanism of the ultrafast crystal growth of pure metals from their melts. *Nat. Mater.* **2018**, *1*, 881.

(10) Greene, L. E.; Yuhas, B. D.; Law, M.; Zitoun, D.; Yang, P. Solution-grown zinc oxide nanowires. *Inorg. Chem.* **2006**, *45* (19), 7535−7543.

(11) Banerjee, D.; Jo, S. H.; Ren, Z. F. Enhanced field emission of ZnO nanowires. *Adv. Mater.* **2004**, *16* (22), 2028−2032.

(12) Shen, M.; Han, A.; Wang, X.; Ro, Y. G.; Kargar, A.; Lin, Y.; Guo, H.; Du, P.; Jiang, J.; Zhang, J. Atomic scale analysis of the enhanced electro-and photo-catalytic activity in high-index faceted porous NiO nanowires. *Sci. Rep.* **2015**, *5*, 8557.

(13) Li, C.; Sato, T.; Yamauchi, Y. Electrochemical Synthesis of One-Dimensional Mesoporous Pt Nanorods Using the Assembly of Surfactant Micelles in Confined Space. *Angew. Chem., Int. Ed.* **2013**, *52* (31), 8050−8053.

(14) Liu, L.; Pippel, E.; Scholz, R.; Gösele, U. Nanoporous Pt− Co alloy nanowires: fabrication, characterization, and electrocatalytic properties. *Nano Lett.* **2009**, *9* (12), 4352−4358.

(15) Li, H.; Misra, A.; Baldwin, J. K.; Picraux, S. Synthesis and characterization of nanoporous Pt−Ni alloys. *Appl. Phys. Lett.* **2009**, *95* (20), 201902.

(16) Shui, J.-L.; Zhang, J.-W.; Li, J. C. Making Pt-shell Pt 30 Ni 70 nanowires by mild dealloying and heat treatments with little Ni loss. *J. Mater. Chem.* **2011**, *21* (17), 6225−6229.

(17) Jin, H.-J.; Wang, X.-L.; Parida, S.; Wang, K.; Seo, M.; Weissmüller, J. r. Nanoporous Au− Pt alloys as large strain electrochemical actuators. *Nano Lett.* **2010**, *10* (1), 187−194.

(18) Tominaka, S.; Hayashi, T.; Nakamura, Y.; Osaka, T. Mesoporous PdCo sponge-like nanostructure synthesized by electrodeposition and dealloying for oxygen reduction reaction. *J. Mater. Chem.* **2010**, *20* (34), 7175−7182.

(19) Schuettler, M.; Doerge, T.; Wien, S.; Becker, S.; Staiger, A.; Hanauer, M.; Kammer, S.; Stieglitz, T. Cytotoxicity of platinum black. *Proc. of FES Society* **2005**, 343−345.

(20) Erlebacher, J.; Aziz, M. J.; Karma, A.; Dimitrov, N.; Sieradzki, K. Evolution of nanoporosity in dealloying. *Nature* **2001**, *410* (6827), 450−453.

(21) Graf, M.; Roschning, B.; Weißmüller, J. Nanoporous gold by alloy corrosion: Method-structure-property relationships. *J. Electrochem. Soc.* **2017**, *164* (4), C194−C200.

(22) Uguz, I.; Ganji, M.; Hama, A.; Tanaka, A.; Inal, S.; Youssef, A.; Owens, R. M.; Quilichini, P. P.; Ghestem, A.; Bernard, C. Autoclave Sterilization of PEDOT: PSS Electrophysiology Devices. *Adv. Healthcare Mater.* **2016**, *5*, 3094.

(23) Khodagholy, D.; Gelinas, J. N.; Thesen, T.; Doyle, W.; Devinsky, O.; Malliaras, G. G.; Buzsáki, G. NeuroGrid: recording action potentials from the surface of the brain. *Nat. Neurosci.* **2015**, *18* (2), 310−315.

(24) Ganji, M.; Elthakeb, A. T.; Tanaka, A.; Gilja, V.; Halgren, E.; Dayeh, S. A. Scaling Effects on the Electrochemical Performance of poly (3, 4-ethylenedioxythiophene (PEDOT), Au, and Pt for Electrocorticography Recording. *Adv. Funct. Mater.* **2017**, *27* (42), 1703018.

DOI: 10.1021/acs.nanolett.9b02296
Nano Lett. XXXX, XXX, XXX−XXX

(25) Ganji, M.; Elthakeb, A. T.; Tanaka, A.; Gilja, V.; Halgren, E.; Dayeh, S. A. Scaling Effects on the Electrochemical Performance of poly (3, 4-ethylenedioxythiophene (PEDOT), Au, and Pt for Electrocorticography Recording. *Adv. Funct. Mater.* **2017**, *27* (42), 1703018.
(26) Flesher, S. N.; Collinger, J. L.; Foldes, S. T.; Weiss, J. M.; Downey, J. E.; Tyler-Kabara, E. C.; Bensmaia, S. J.; Schwartz, A. B.; Boninger, M. L.; Gaunt, R. A. Intracortical microstimulation of human somatosensory cortex. *Sci. Transl. Med.* **2016**, *8* (361), 361ra141−361ra141.
(27) Ganji, M.; Kaestner, E.; Hermiz, J.; Rogers, N.; Tanaka, A.; Cleary, D.; Lee, S. H.; Snider, J.; Halgren, M.; Cosgrove, G. R. Development and Translation of PEDOT: PSS Microelectrodes for Intraoperative Monitoring. *Adv. Funct. Mater.* **2018**, *28* (12), 1700232.
(28) Sessolo, M.; Khodagholy, D.; Rivnay, J.; Maddalena, F.; Gleyzes, M.; Steidl, E.; Buisson, B.; Malliaras, G. G. Easy-to-fabricate conducting polymer microelectrode arrays. *Adv. Mater.* **2013**, *25* (15), 2135−2139.
(29) Uguz, I.; Ganji, M.; Hama, A.; Tanaka, A.; Inal, S.; Youssef, A.; Owens, R. M.; Quilichini, P. P.; Ghestem, A.; Bernard, C. Autoclave sterilization of PEDOT: PSS electrophysiology devices. *Adv. Healthcare Mater.* **2016**, *5* (24), 3094−3098.
(30) Hermiz, J.; Rogers, N.; Kaestner, E.; Ganji, M.; Cleary, D.; Snider, J.; Barba, D.; Dayeh, S.; Halgren, E.; Gilja, V. *A Clinic Compatible, Open Source Electrophysiology System*; IEEE EMBC: Orlando, FL, 2016; Vol. *38*.
(31) Siegle, J. H.; López, A. C.; Patel, Y. A.; Abramov, K.; Ohayon, S.; Voigts, J. Open Ephys: an open-source, plugin-based platform for multichannel electrophysiology. *Journal of neural engineering* **2017**, *14* (4), 045003.
(32) Paxinos, G.; Franklin, K. B. J. *The Mouse Brain in Stereotaxic Coordinates*, 2nd ed.; Academic Press: San Diego, 2001.

DOI: 10.1021/acs.nanolett.9b02296
Nano Lett. XXXX, XXX, XXX−XXX

Supporting Information

Selective Formation of Porous Pt Nanorods for Highly Electrochemically Efficient Neural Electrode Interfaces

Mehran Ganji,[1] Angelique C. Paulk,[2] Jimmy C. Yang,[2] Nasim W. Vahidi,[1] Sang Heon Lee,[1] Ren Liu,[1] Lorraine Hossain,[3] Ezequiel M. Arneodo,[4] Martin Thunemann,[4] Michiko Shigyo,[6] Atsunori Tanaka,[3] Sang Baek Ryu,[7] Seung Woo Lee,[7] Youngbin Tchoe,[1] Martin Marsala,[6] Anna Devor,[5] Daniel R. Cleary,[8] Joel R. Martin,[8] Hongseok Oh,[1] Vikash Gilja,[1] Timothy Q. Gentner,[4] Shelley I. Fried,[7,9] Eric Halgren,[5] Sydney S. Cash,[2] and Shadi A. Dayeh[1,2,10]*

[1]Department of Electrical and Computer Engineering, University of California San Diego La Jolla, California 92093, USA

[2]Department of Neurology, Massachusetts General Hospital, Boston, Massachusetts 02114

[3]Materials Science and Engineering Program, University of California San Diego, La Jolla, California 92093, USA

[4]Department of Neurosciences, University of California San Diego, La Jolla, California, 92093, USA

[5]Department of Radiology and Neurosciences, University of California San Diego, La Jolla, California, 92093, USA

[6]Department of Anesthesiology, University of California, San Diego (UCSD), La Jolla, CA 92037, USA.

[7]Department of Neurosurgery, Massachusetts General Hospital, Boston, Massachusetts 02114.

[8]Department of Neurosurgery, University of California, San Diego (UCSD), La Jolla, CA 92037, USA

[9]Boston VA Healthcare System, 150 South Huntington Avenue, Boston, MA 02130

[10]Department of Nanoengineering, University of California San Diego, La Jolla, California 92093, USA

Author to whom correspondence may be addressed: S.A.D. e-mail: sdayeh@eng.ucsd.edu

Keywords: platinum nanorod, clinical, brain, neural interface, neurotechnology

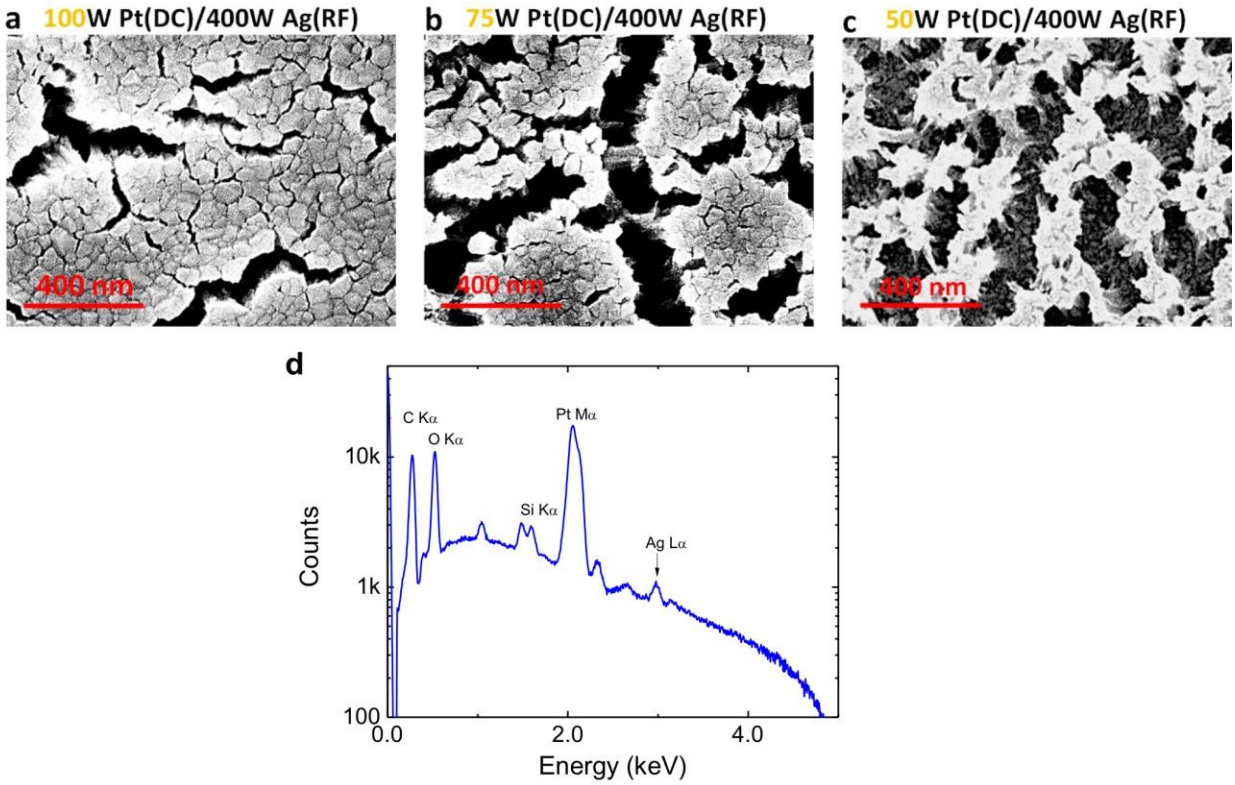

Figure S1: Structural optimization of PtNRs: SEM images of different nanostructured Pt films after chemical etching (de-alloying) using different Pt to Ag concentration ratios of **a)** 100W/ 400W **b)** 75W/ 400W and **c)** 50W/ 400W, resulting in different morphological characteristics. d) Energy dispersive x-ray spectra taken at 89° tilt at the center of the PtNR showing residual Ag with an atomic percentage of 10%.

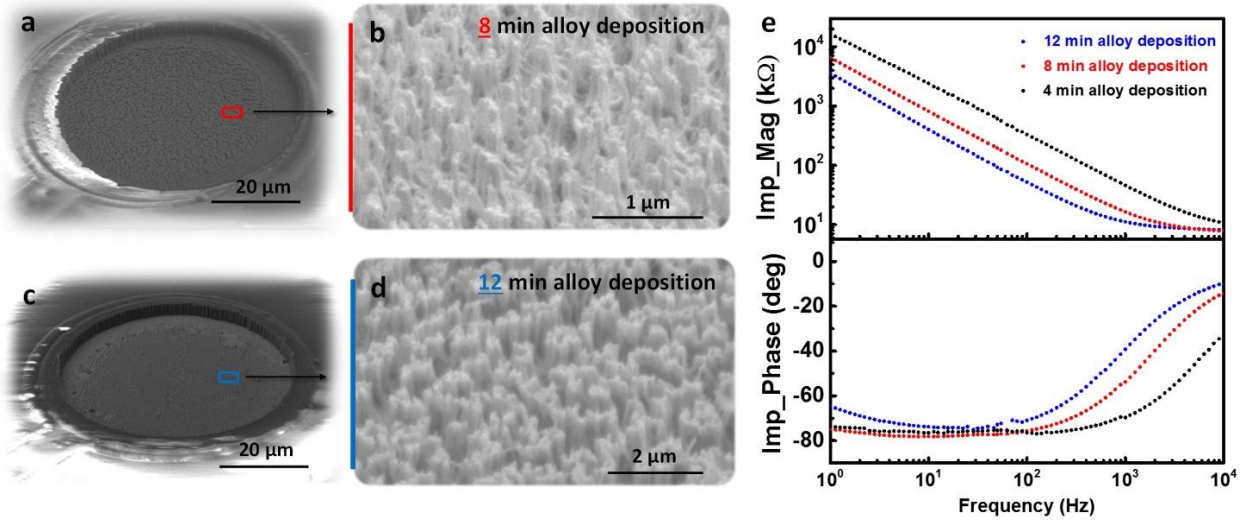

Figure S2: Effect of alloy deposition on the PtNR height: (a) Tilted view SEM image of PtNRs electrode with 8 min co-sputtering deposition, resulting in ~500 nm tall PtNRs **(b)**. **(c)** Tilted view

SEM image of PtNRs electrode with 16 min co-sputtering deposition, resulting in ~1 µm tall PtNRs **(d)**. Electrochemical impedance spectroscopy of various PtNRs electrodes (D=50 µm) with different alloy deposition and PtNRs heights, resulting in different magnitude and phase impedance spectra.

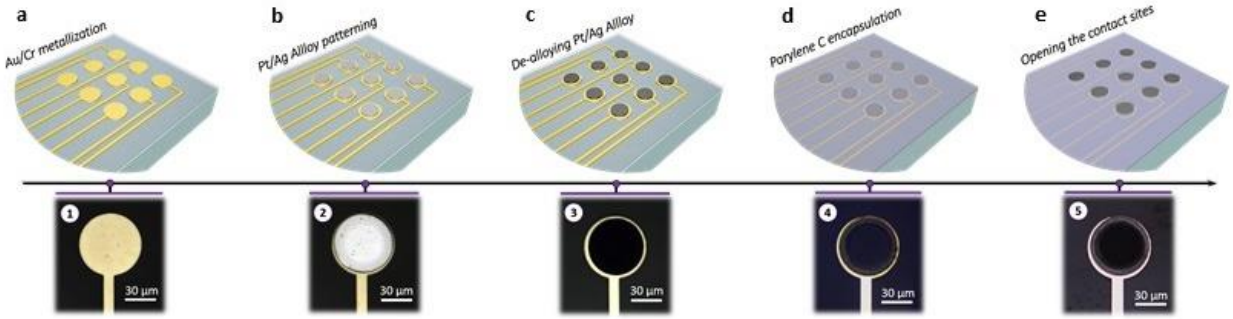

Figure S3: Fabrication flow of the PtNRs-based microelectrodes: a) Au/Cr contacts and leads metallization. **b)** Selective AgPt alloy deposition on sensing sites using co-sputtering deposition system **c)** selective PtNRs formation on electrode sites after chemical de-alloying in nitric acid at 60 C°. **d)** Deposition of second passivation parylene C layer. **e)** Selective oxygen plasma etching of parylene C layer on top of microcontacts and PtNR exposure.

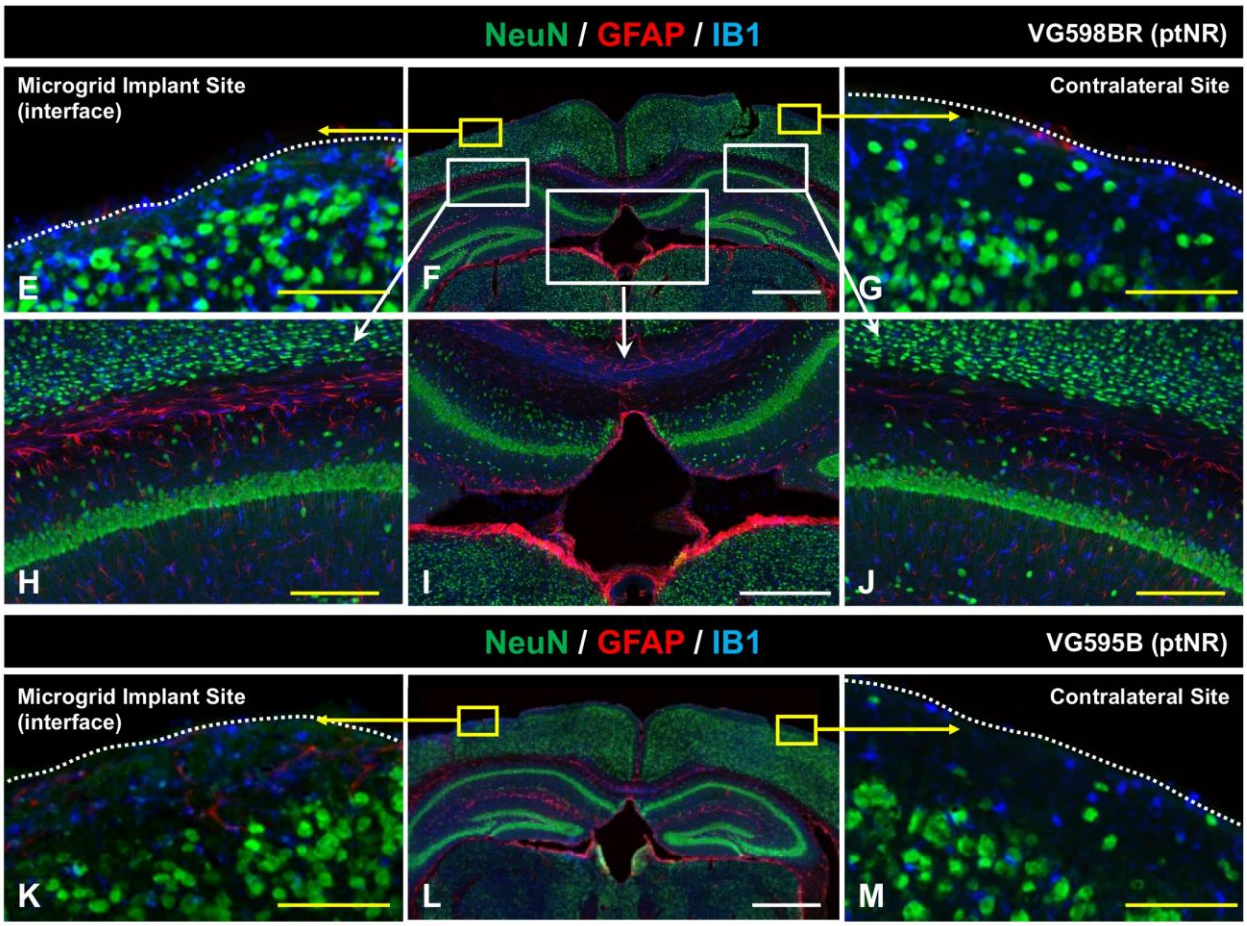

Figure S4: Biocompatibility and safety of cortical-surface PtNR microgrid implant in in two mice, VG598BR (E-J) and VG595B (K-M). In adult anesthetized mice a bur hole was drilled into skull and PtNR microgrid placed on the surface of motor cortex. Dura was cut-opened. After implants animals survived for 42 days and perfusion-fixed with 4% paraformaldehyde. **(A, B)** Intraoperative images taken just after placement of microgrid implants. **(C, D)** Images of cortical surface with implanted microgrid just after perfusion fixation. No fibrotic changes were seen. **(E-M)** Immunofluorescence images taken from coronal brain sections of two animals implanted with PtNR microgrids and stained with NeuN, GFAP and IB1 antibodies. Except of a slight indentation of the cortical surface at the site of microgrid implant near normal neuronal and glial morphology and staining pattern were seen when compared to contralateral non-implanted site. NeuN-stained neurons in cortical superficial layers as well as in hippocampal CA1 sector showed normal appearance with no detectable degeneration (comparing Micogrid Implant Site vs. Contralateral Site). Similarly, a comparable staining pattern for IB1 and GFAP were seen. **Scale bars:** E, G, K, M- 100 µm, F, L- 1 mm, H, L- 200 µm, I- 500 µm.

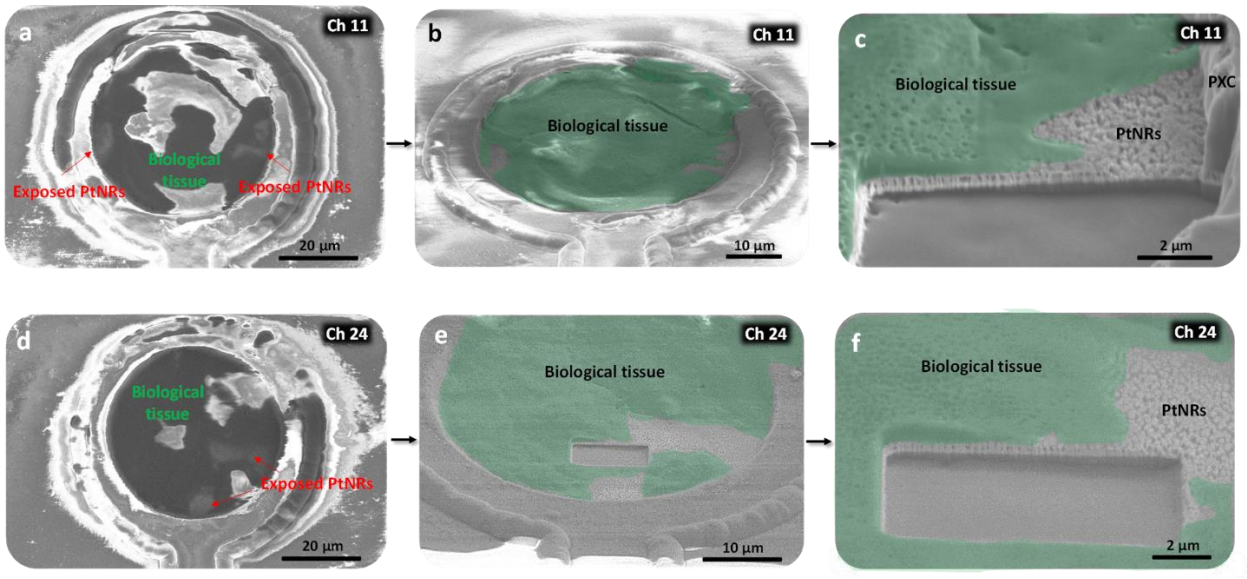

Figure S5: Examining PtNR morphology after 42 days implant in a mouse brain: Top view **(a, d)** and Titled view **(b, e)** SEM image of the ex-planted PtNR electrode (ch 11, ch 24). Cross-sectional SEM image **(c, f)** at sliced PtNR electrode surface, demonstrating a stable PtNRs film condition after ex-planation (42 days) with partial coverage with biological tissue.

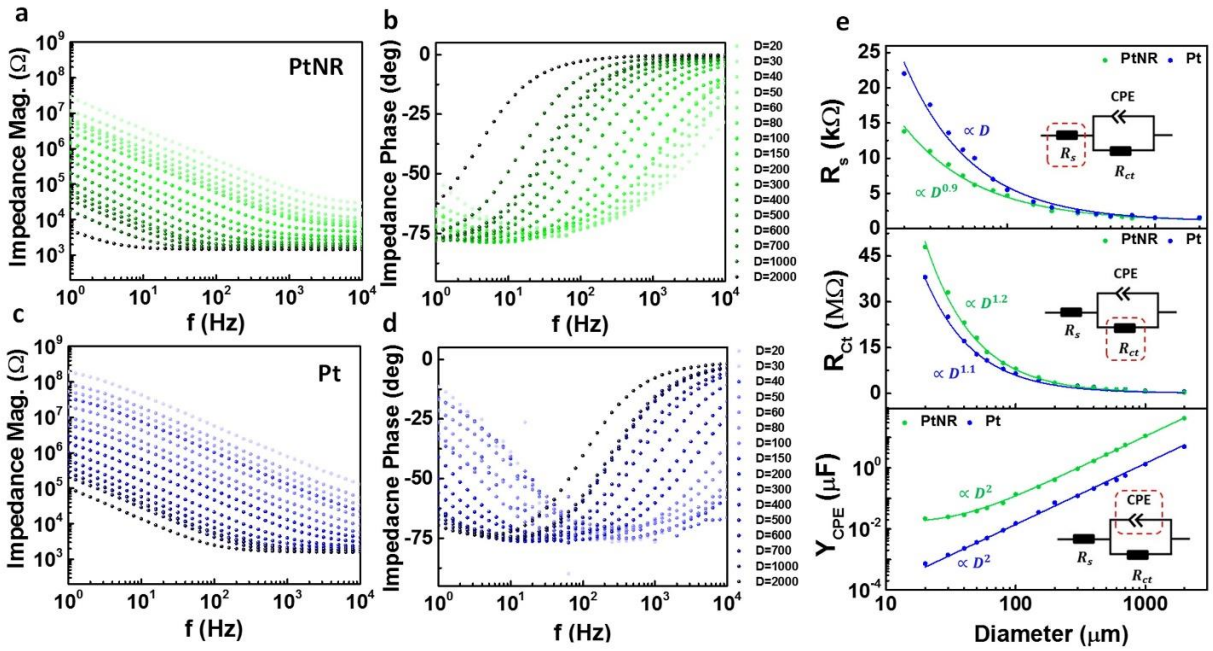

Figure S6: Electrochemical impedance measurements and analyses for Pt and PtNRs electrodes as a function of diameter: Electrochemical impedance magnitude and phase spectroscopy of PtNR **(a** and **b)** and Pt **(c** and **d)** electrodes with varying diameters ranging from 2,000 μm to 20 μm. **e)** Equivalent circuit model and corresponding small signal components of different small signal components (highlighted in red box in insets) for PtNR (blue) and Pt (green) electrodes.

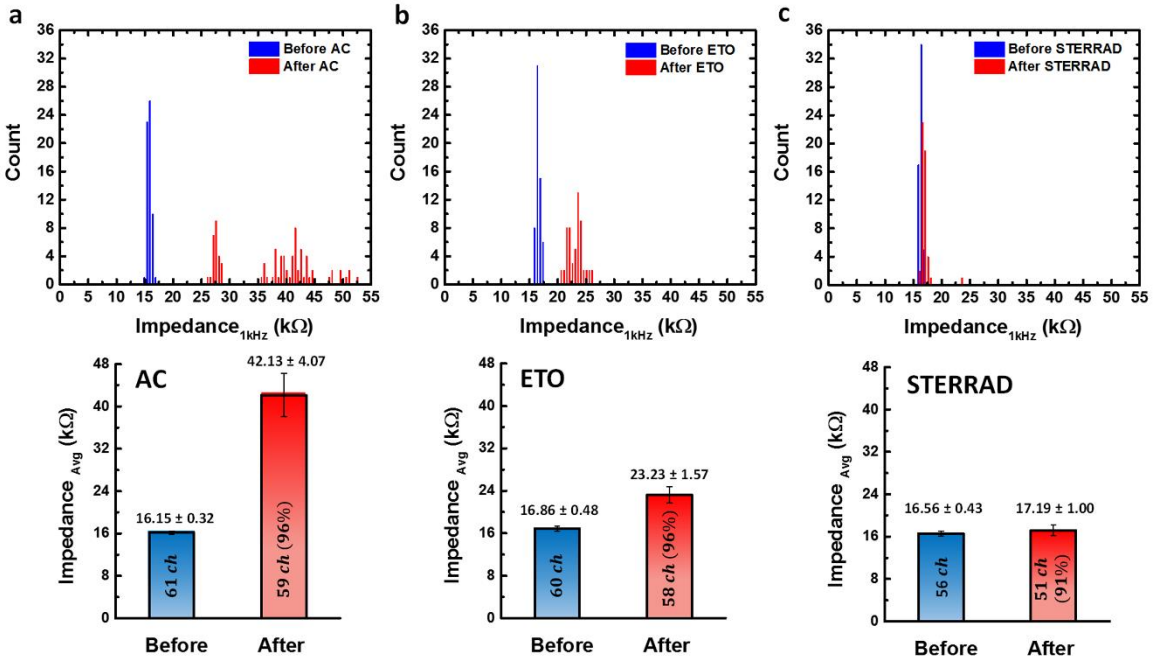

Figure S7: Sterilization effects on the PtNR electrode impedance: 1 kHz electrochemical impedance magnitude histogram of PtNR channels and corresponding statistics (AVG + STD) before (blue) and after (red) Autoclave **(a)**, ETO **(b)** and STERRAD **(c)** sterilization techniques. EIS was first performed at UCSD, shipped to MGH for sterilization procedures, and then shipped back to UCSD for EIS measurements. Some channels were non-functional after receiving the devices back at UCSD likely due to failure at the ACF-ribbon/device interface, which was encountered even without devices undergoing the sterilization procedure.

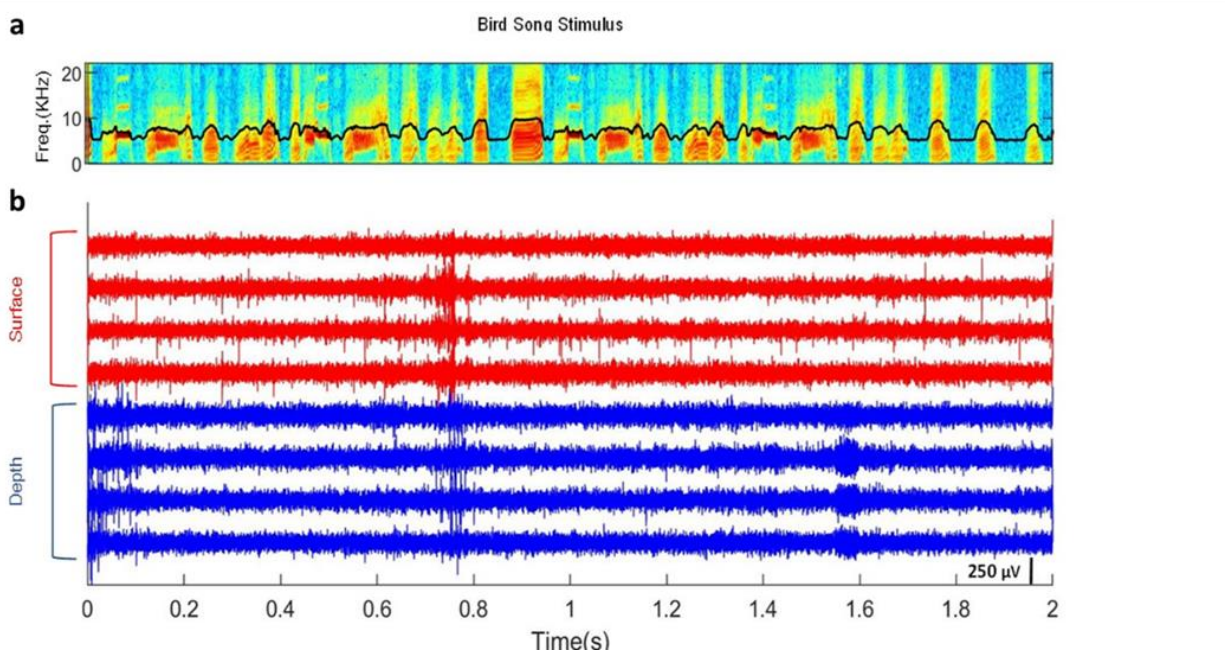

Figure S8: Example of recorded high pass filtered data from surface and depth electrodes: a) Spectrogram of the stimulus of a zebra finch song. The black waveform is the log of power spectrum density (PSD) averaged over 65 frequency bands of spectrogram. **b)** Eight high-pass filtered time series: Four recorded from surface electrodes in red and the other four are recorded from depth electrodes in blue. The black scale bar in bottom right indicates amplitude of 250µV.

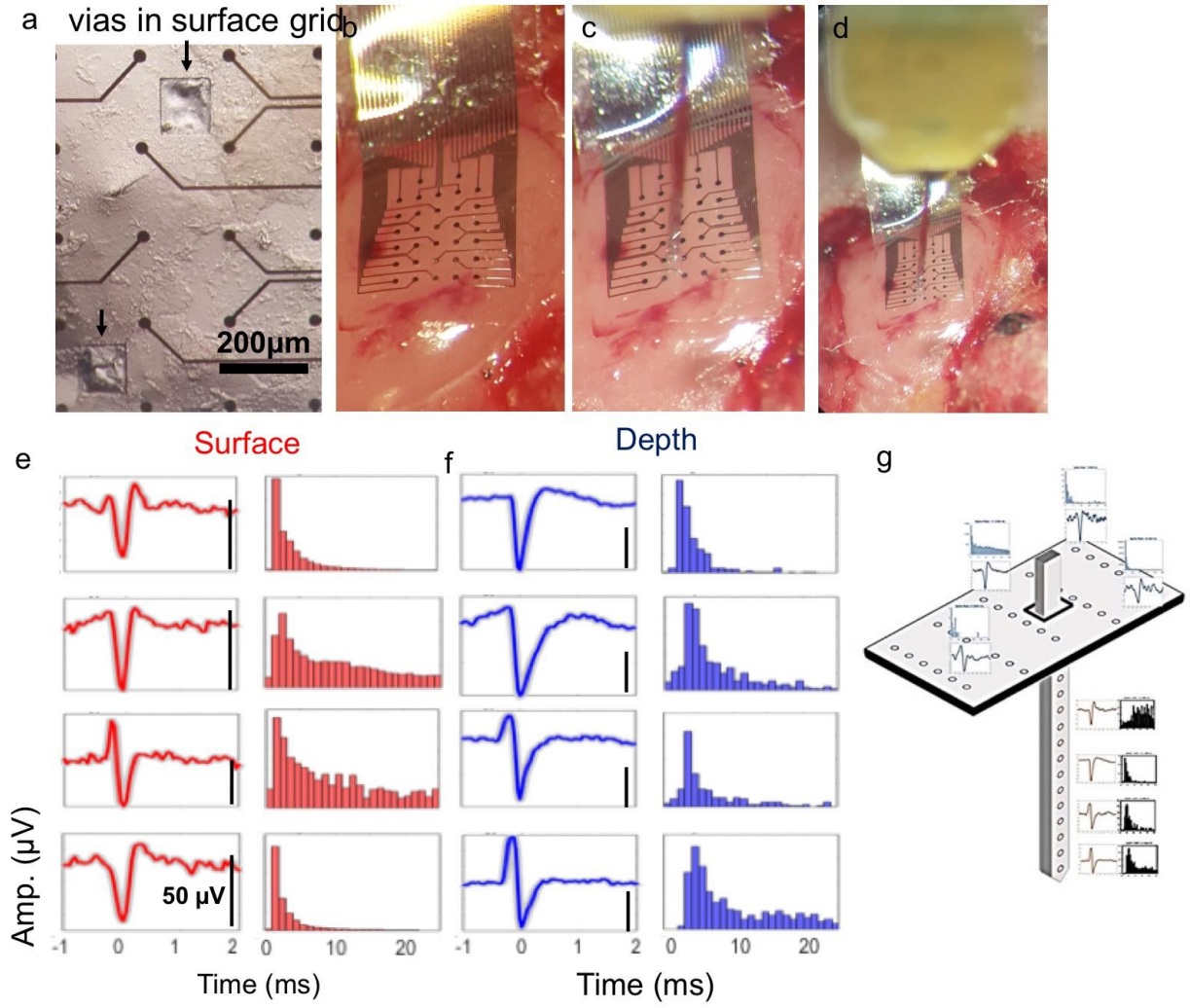

Figure S9: Examples of recorded single cell spike waveforms from surface and depth electrode: a) Zoom-in image showing the via hole created in the surface grid for the insertion of the depth electrode. **b)** Placement of the surface grid on the HVC. **c)** Insertion of the NeruoNexus Si probe* through the proximal via. **d)** An image showing a larger field of view of the preparation. **e)** Single cells recorded spike waveforms from surface electrode. The red waveforms are averages of 20 sampled spike snippets and the scale black bar indicates 50µV in amplitude. Left column are waveforms corresponding inter-spike interval (ISI) histograms in red. **f)** Single cells recorded spike waveforms from depth electrode. The blue waveforms are averages of 20 sampled spike snippets. Left column demonstrates the waveforms corresponding inter-spike interval (ISI) histograms. g) Spatial distribution of the recorded spikes on the surface and the dept electrodes.

*The depth electrode used is a Neuronexus Si probe (a1x16-5mm-50-413) and was placed between 450-550um into the cortex, 0 rostro-caudal, and 2400um lateral to Y-Sinus. The depth electrode is inserted into a 200µm x 200µm etched window in the parylene C layer of the PtNR ECoG electrode.

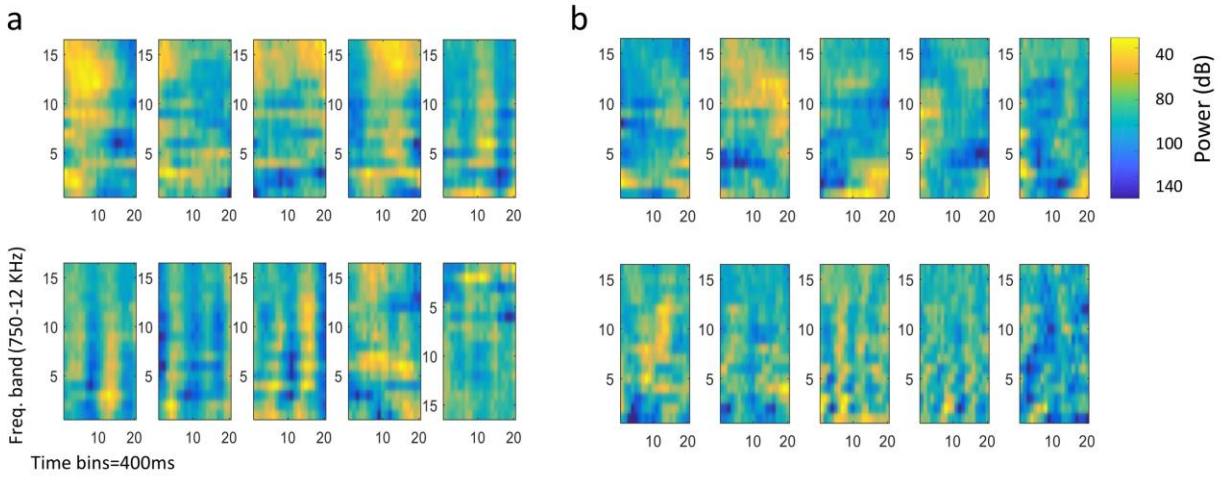

Figure S10: Examples of extracted CRFs from a cortical surface cell. a) 10 most significant facilitatory receptive fields of a single cell. **b)** 10 most significant excitatory receptive fields. This demonstrates that cells recorded with PtNR microelectrodes are of high quality enabling us to extract low noise receptive fields from them.

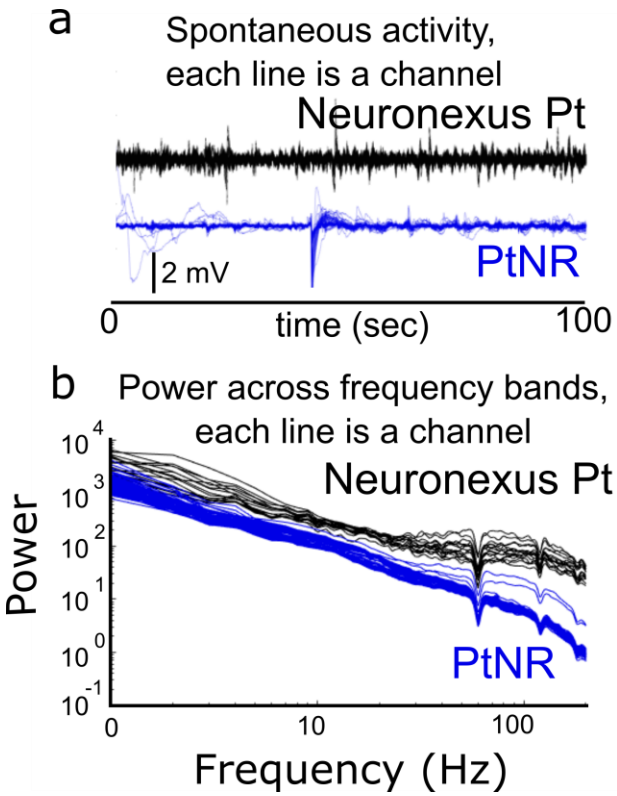

Figure S11: Comparisons between PtNR and Neuronexus Pt electrodes. **a)** Voltage traces for the Neuronexus (black lines) and PtNR (blue lines) electrodes for 100 seconds of recordings. Each line is a different channel for the different electrode types. The recordings were performed sequentially over the same area of NHP cortex. Both recordings were decimated to 1000 Hz with line noise removed and high pass filtered at 1 Hz. **B)** Log power over frequencies of three minutes of spontaneously recorded data from the Neuronexus (black lines) and PtNR (blue lines) electrodes. The power was calculated using wavelet analysis which is the real value for the Morlet wavelet coefficient amplitude.